iScience

CellPress
OPEN ACCESS

Article

Clathrin-mediated endocytosis cooperates with bulk endocytosis to generate vesicles

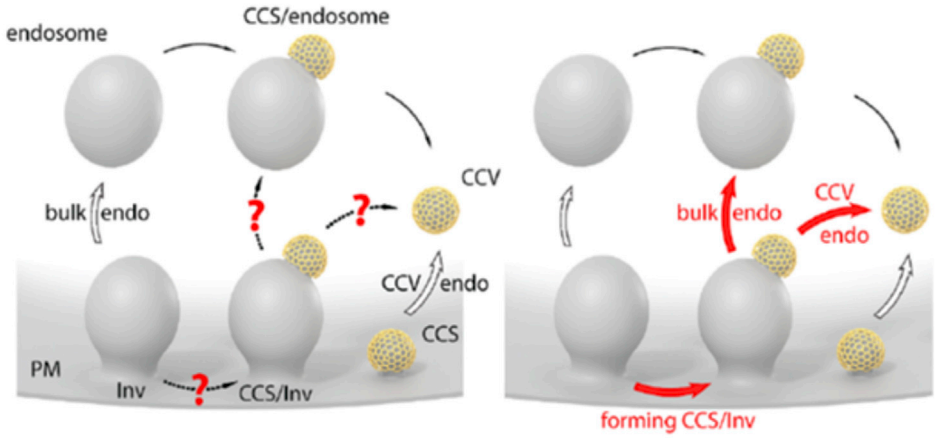

Endocytic pathways (red) in question

Endocytic pathways (red) supported by current work

Abbreviations: CCS, clathrin-coated structure; CCV, clathrin-coated vesicle; endo, endocytosis; Inv, membrane invagination; PM, Plasma membrane.

Gianvito Arpino, Agila Somasundaram, Wonchul Shin, ..., Oleg Shupliakov, Justin W. Taraska, Ling-Gang Wu

justin.taraska@nih.gov (J.W.T.)
wul@ninds.nih.gov (L.-G.W.)

Highlights

Bulk membrane invaginations are primary sites for clathrin-coated pit formation

Invaginations are preferred over flat membrane for clathrin-coated pit formation

Clathrin-coated vesicle formation from membrane invagination is suggested

Clathrin-mediated and bulk endocytosis collaborate to enhance endocytic capacity

Arpino et al., iScience 25, 103809
February 18, 2022 © 2022
https://doi.org/10.1016/j.isci.2022.103809

iScience

CellPress
OPEN ACCESS

Article

Clathrin-mediated endocytosis cooperates with bulk endocytosis to generate vesicles

Gianvito Arpino,[1] Agila Somasundaram,[2] Wonchul Shin,[1] Lihao Ge,[1] Seth Villareal,[1] Chung Yu Chan,[1] Uri Ashery,[3] Oleg Shupliakov,[4,5] Justin W. Taraska,[2,*] and Ling-Gang Wu[1,6,*]

SUMMARY

Clathrin-mediated endocytosis, the most prominent endocytic mode, is thought to be generated primarily from relatively flat patches of the plasma membrane. By employing conventional and platinum replica electron microscopy and super-resolution STED microscopy in neuroendocrine chromaffin cells, we found that large Ω-shaped or dome-shaped plasma membrane invaginations, previously thought of as the precursor of bulk endocytosis, are primary sites for clathrin-coated pit generation after depolarization. Clathrin-coated pits are more densely packed at invaginations rather than flat membranes, suggesting that invaginations are preferred sites for clathrin-coated pit formation, likely because their positive curvature facilitates coated-pit formation. Thus, clathrin-mediated endocytosis closely collaborates with bulk endocytosis to enhance endocytic capacity in active secretory cells. This direct collaboration between two classically independent endocytic pathways is of broad importance given the central role of both clathrin-mediated endocytosis and bulk endocytosis in neurons, endocrine cells, immune cells, and many other cell types throughout the body.

INTRODUCTION

Endocytosis mediates key biological processes, such as intracellular trafficking, nutrient uptake, viral entry, and vesicle recycling that sustains exocytosis in neurons and endocrine cells (Gan and Watanabe, 2018; Kononenko and Haucke, 2015; Saheki and De Camilli, 2012). The most prominent endocytic mode in eukaryotic cells is clathrin-mediated endocytosis, which generates clathrin-coated patches, pits, and vesicles (~30–100 nm) from the plasma membrane (PM). Because clathrin-coated pits or patches are observed primarily at flat sections of the PM, clathrin-mediated endocytosis is thought to be generated from flat PM regions (Gan and Watanabe, 2018; Heuser and Reese, 1973; Kononenko and Haucke, 2015; Saheki and De Camilli, 2012; Watanabe et al., 2013). A study three decades ago proposed that clathrin-coated vesicles can also be generated from preformed PM invaginations (Takei et al., 1996). In this pioneering study, however, the model was based on only a few examples without robust statistics. The main data supporting this proposal (see Figure 6C in Takei et al., 1996) was not entirely convincing for three reasons: 1) the pit appeared as a round vesicle separated from the large membrane invagination – the connection between the pit and the large membrane invagination is unclear; 2) clathrin-coating on the pit or vesicle was not typical and thus fully convincing; and 3) it was observed in a highly unphysiological conditions: in the presence of a powerful inhibitor of fission (GTP-γS) that promotes clathrin coating on pits that could not undergo fission (Ferguson et al., 2007), and in synaptosomes (isolated nerve terminals) subjected to severing between axons and nerve terminals that are no longer used for endocytosis studies today. Thus, the proposal that clathrin-coated pits and vesicles in secretory cells can be generated from large membrane invagination is not fully supported with, and remains to be proved by, quantitative and high-resolution microscopy in physiologically intact cells without fission inhibitors. Whether and to what extent clathrin-coated pits and vesicles are generated from PM invaginations in secretory cells remains unclear.

Here, we studied whether and to what extent clathrin-coated pits and vesicles are generated from large PM invagination using conventional thin section electron microscopy (EM), platinum replica EM, and super-resolution stimulated emission depletion (STED) microscopy in primary neuroendocrine chromaffin cells commonly used for exo-endocytosis studies (Wu et al., 2014a). We provided multimodal quantitative data showing that large PM invaginations, the membrane curvature produced by bulk endocytosis, are a

[1]National Institute of Neurological Disorders and Stroke, Bethesda, MD, USA

[2]National Heart, Lung, and Blood Institute, Bethesda, MD, USA

[3]Life Science Faculty, Sagol School of Neuroscience, Tel Aviv University, Tel Aviv, Israel

[4]Department of Neuroscience, Karolinska Institutet, Stockholm, Sweden

[5]Institute of Translational Biomedicine, St Petersburg State University, St Petersburg, Russia

[6]Lead contact

*Correspondence: justin.taraska@nih.gov (J.W.T.), wul@ninds.nih.gov (L.-G.W.)

https://doi.org/10.1016/j.isci.2022.103809

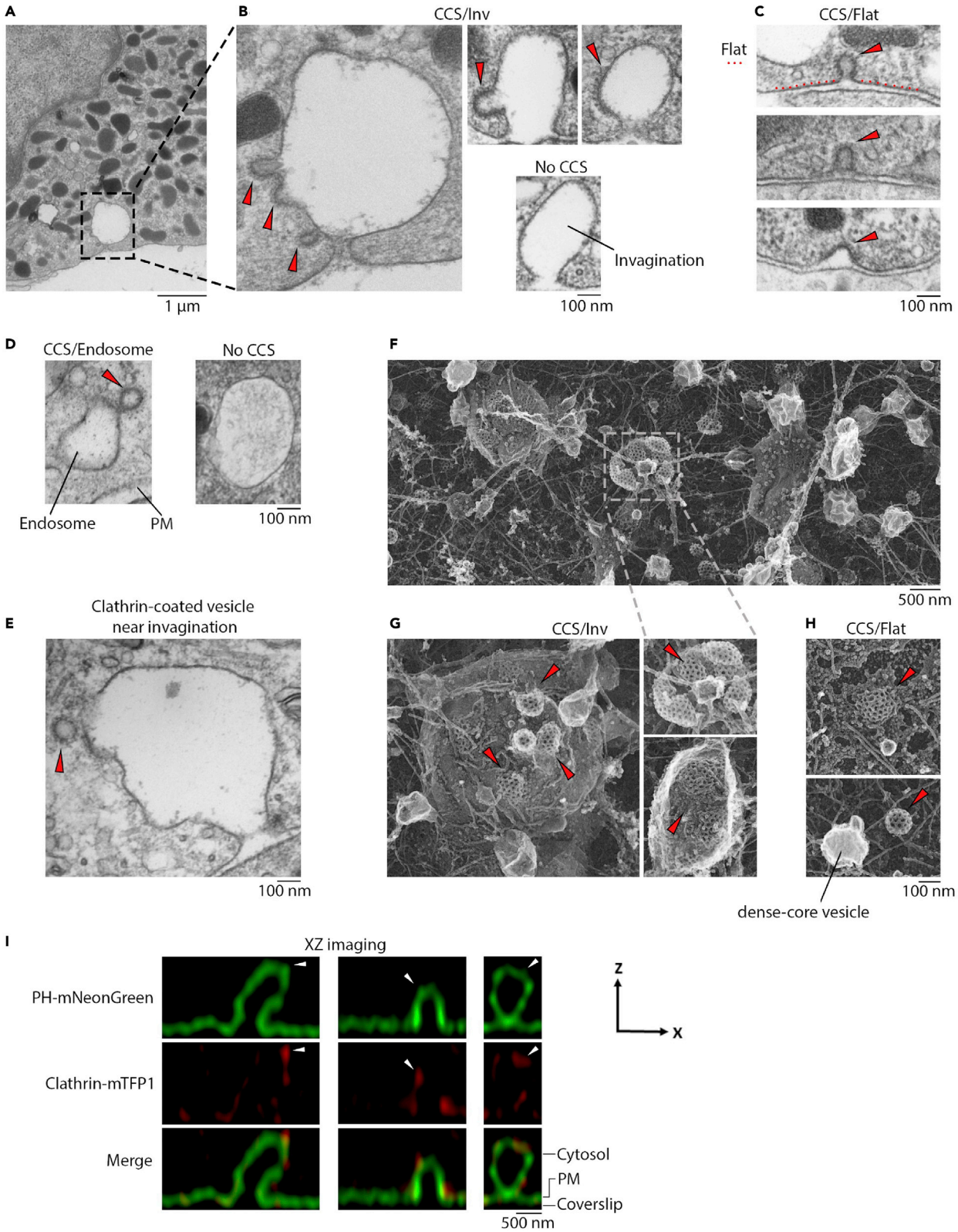
A
B
CCS/Inv
No CCS
Invagination
1 µm
100 nm
C
CCS/Flat
Flat
100 nm
D
CCS/Endosome
No CCS
Endosome
PM
100 nm
F
500 nm
E
Clathrin-coated vesicle
near invagination
100 nm
G
CCS/Inv
H
CCS/Flat
100 nm
dense-core vesicle
I
XZ imaging
PH-mNeonGreen
Clathrin-mTFP1
Merge
Z
X
Cytosol
PM
Coverslip
500 nm

Figure 1. Clathrin-coated structures at large invaginations or flat PM

(A–E) Conventional EM images from cells in 70 mM KCl for 90 s. (A) low magnification, dash square enlarged in (B). (B) sampled CCS/Inv (triangles) – clathrin-coated pits or plaques associated with large invaginations (one invagination associated with no CCS is also shown). (C) sampled CCS/Flat (triangles) – clathrin-coated pits flanked by flat PM (dotted line outlines a flat membrane). (D) endosome-like structures associated with a CCS (left) or without CCS (right). (E) a clathrin-coated vesicle (triangle) near a large invagination.

(F–H) Platinum replica EM images from cells unroofed 45 s after KCl (70 mM) application. (F) low magnification image (dash square enlarged in G). (G) sampled CCS/Inv, clathrin-coated pits (triangles) at the top of membrane invagination. (H) sampled CCS/Flat, clathrin-coated membrane pits (triangles) surrounded by flat PM. The bright spot (lower) may correspond to a dense-core vesicle.

(I) STED XZ-plane images of PH_{mNG}, Clathrin-mTFP1 (red, pseudocolor), and merge images showing three large Ω-shaped profiles associated with clathrin-mTFP1 puncta. Triangles indicate PH_{mNG}-labeled membrane protrusions (potential pits) overlapping clathrin-mTFP1 puncta. Cytosol, PM, and coverslip locations are labeled.

major platform for producing clathrin-coated pits and vesicles. This finding suggests that two seemingly independent forms of endocytosis, clathrin-mediated endocytosis, and bulk endocytosis, work together to enhance endocytic capacity. Such a collaboration is of broad importance, given that clathrin-mediated endocytosis is essential for the life of most eukaryotic cells (Mettlen et al., 2018), and bulk endocytosis is a major form of endocytosis in secretory cells and beyond (Clayton et al., 2008; Kononenko et al., 2014; Richards et al., 2000; Roberts et al., 2020; Watanabe et al., 2013; Wu et al., 2014a; Wu and Wu, 2007).

RESULTS

Clathrin-coated structures at large invaginations or flat membrane: conventional EM observation

With conventional EM, we examined primary cultured bovine adrenal chromaffin cells in control conditions and at 90 s after applying 70 mM KCl to induce exo-endocytosis (Shin et al., 2018). At single cell cross sections (e.g., Figure 1A), we observed clathrin-coated structures (CCSs), including clathrin-coated deep or shallow pits or patches, at three membrane sites: 1) on the top or side of large Ω-shaped or dome-shaped PM invaginations (Inv, height >300 nm), termed CCS/Inv (Figure 1B), 2) alone, but connected with nearby flat PM, termed CCS/Flat (Figure 1C), and 3) at cytosolic endosome-like structure (Figure 1D). CCSs were not found at every invagination or endosome-like structure (Figures 1B and 1D), likely in part because the section (70-nm) was too thin to include the entire structure. We also observed clathrin-coated vesicles within 100 nm of membrane invagination (Figure 1E), suggesting that clathrin-coated vesicles may be generated from CCS/Inv.

Verifying CCSs at membrane invagination with platinum replica EM and STED imaging

With conventional EM, we identified CCSs based on typical dense structures of clathrin coatings (Figures 1A–1E). Here we verified this method with two additional approaches. First, we performed platinum replica EM on cells unroofed 45 s after applying KCl (70 mM). Unroofing preserved only PM-associated structures, including honeycomb shaped clathrin-coated plaques or pits that were unequivocally identified with platinum replica EM (Figure 1F) (Hirokawa and Heuser, 1981; Sochacki et al., 2017, 2021). We observed clathrin-coated pits on top of invaginations (Figure 1G, CCS/Inv, n > 30, from 11 cells) or alone, but surrounded by flat PM (Figure 1H, CCS/Flat, n > 30, 11 cells). Many large smooth uncoated vesicles with bright interiors likely corresponding to dense-core vesicles were also observed (e.g., Figure 1H).

Second, we examined CCSs in live cells overexpressed with clathrin light chain attached to mTFP1 (clathrin-mTFP1), and mNeonGreen attached to phospholipase C delta PH domain (PH_{mNG}) that binds to PM PtdIns(4,5)P2 (Lomasney et al., 1996; Zhao et al., 2016). STED XZ-plane imaging of clathrin-mTFP1/PH_{mNG} revealed clathrin-mTFP1 puncta associated with large PH_{mNG}-labeled Ω-shape structures or flat PH_{mNG}-labeled PM (Figure 1I, 94 cells). On the top or side of large Ω-profiles, there were small PH_{mNG}-labeled protrusions overlapping with clathrin-mTFP1 puncta (n = 30 events), consistent with clathrin-coated pits or plaques at large invaginations. These observations were from resting cells. We could not resolve the pit shape because of the STED resolution limit (~60–80 nm on X axis, ~150–200 nm on z axis) (Shin et al., 2018). With this resolution limit, we could not reliably observe the dynamics of clathrin-coated pit formation or scission.

PM invagination is a major platform for CCS production

Having identified CCS/Inv and CCS/Flat with conventional EM, platinum replica EM and STED imaging (Figure 1), we quantified conventional-EM-observed CCS/Inv and CCS/Flat. At rest, CCS/Inv number

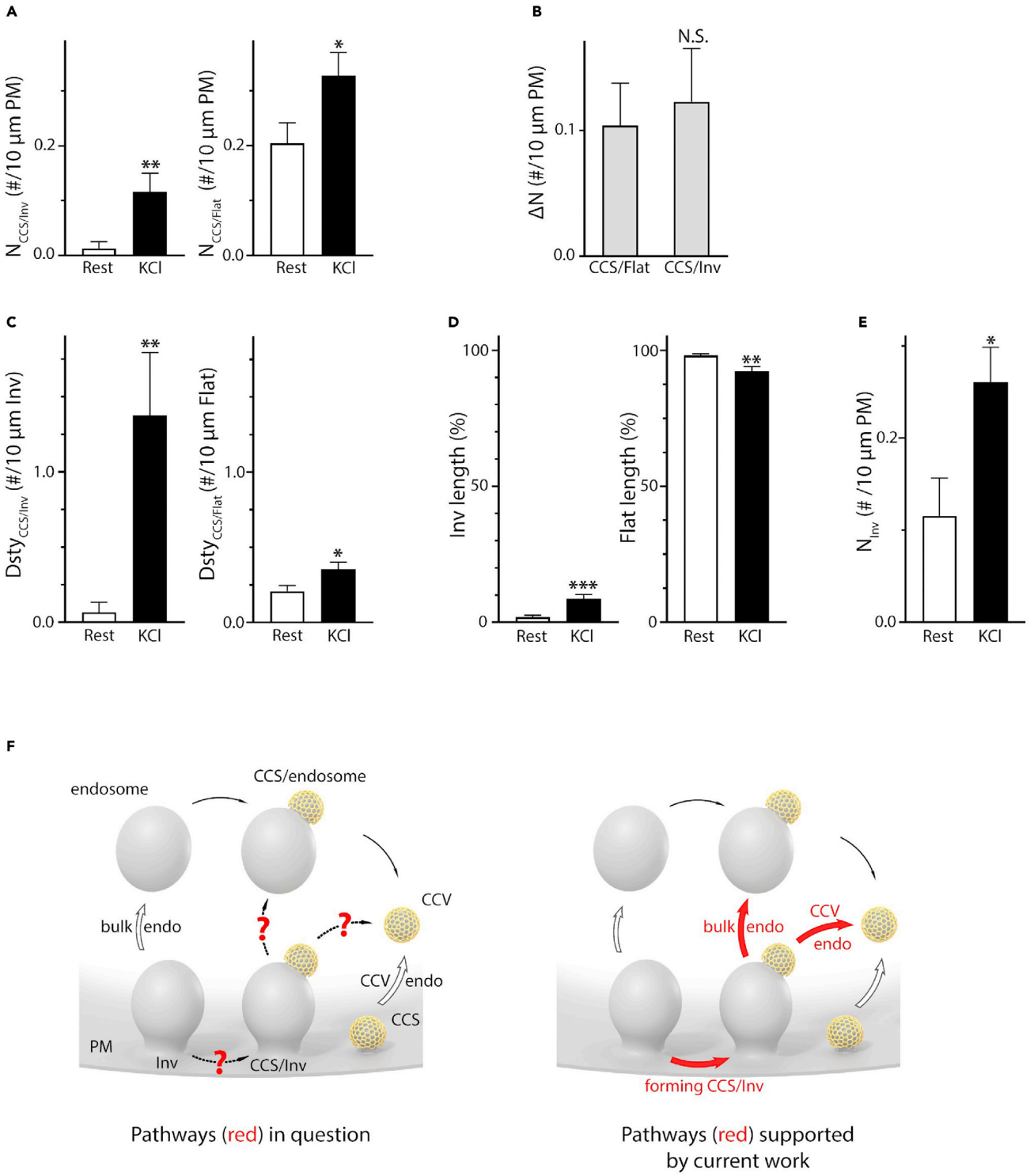

Figure 2. Invagination for clathrin-coated structure generation

(A) $N_{CCS/Inv}$ [CCS/Inv number (#) per 10 µm PM] and $N_{CCS/Flat}$ (CCS/Flat # per 10 µm PM) in resting conditions (Rest, 40 sections, three adrenal glands) or 90 s KCl (70 mM) (40 sections, nine adrenal glands). Data from conventional EM, expressed as mean +SEM; *: $p < 0.05$; **: $p < 0.01$, ***: $p < 0.001$, NS.: $p > 0.05$; Student's t test (apply to A–E).

(B) $\Delta N_{CCS/Inv}$ (net $N_{CCS/Inv}$ increase, # per 10 µm PM) and $\Delta N_{CCS/Flat}$ ($N_{CCS/Flat}$) induced by KCl application (compared to resting condition).

(C) $Dsty_{SCC/Inv}$ (CCS/Inv number per 10 µm Inv) and $Dsty_{CCS/Flat}$ (CCS/Flat number per 10 µm flat PM) at Rest (40 sections) or KCl (40 sections).

Figure 2. *Continued*

(D) Invagination (Inv, left) or Flat PM (right) length percentage at Rest (40 sections) or KCl (40 sections). Percentage is normalized to total PM length.

(E) Number of invaginations (N_{Inv}, per 10 μm PM) at Rest (40 sections) or KCl (40 sections).

(F) Schematic drawings of the traditional model (left) and our new model (right) on the bulk endocytosis (endo) and clathrin-coated vesicle (CCV) endo. Red arrows: new bulk endo and CCV endo derived from the present work; open arrows: traditional bulk endo and CCV endo; black thin arrows: CCV generated from endosome-like structure.

See also Figure S1.

(per unit length of PM), $N_{CCS/Inv}$, was negligible compared to CCS/Flat number ($N_{CCS/Flat}$, Figure 2A). After 70 mM KCl application, $N_{CCS/Inv}$ increased from 0.012 ± 0.012/10 μm (40 sections, at rest) to 0.116 ± 0.033/10 μm (40 sections, KCl), ~10 times increase (Figure 2A, left), whereas $N_{CCS/Flat}$ increased from 0.204 ± 0.037/10 μm (40 sections, at rest) to 0.327 ± 0.042/10 μm (40 sections, KCl), only ~60% increase (Figure 2A, right).

Although KCl application increased $N_{CCS/Inv}$ by a much larger percentage (~10 times) than $N_{CCS/Flat}$ (~60%, Figure 2A), the net increase of $N_{CCS/Inv}$ ($\Delta N_{CCS/Inv}$), calculated as $N_{CCS/Inv}$ after KCl application subtracted by the mean $N_{CCS/Inv}$ at rest, was similar to the net increase of $N_{CCS/Flat}$ ($\Delta N_{CCS/Inv}$, Figure 2B). This result suggests that both CCS/Inv and CCS/Flat are major sources for CCS generation. Consistent with the much larger percentage increase of $N_{CCS/Inv}$ than $N_{CCS/Flat}$ (Figure 2A), CCS/Inv density ($Dsty_{CCS/Inv}$), calculated as the CCS/Inv number per unit length of Inv, increased from 0.066 ± 0.010/10 μm at rest to 1.375 ± 0.420/10 μm after KCl application, ~21 times increase (Figure 2C, left). In contrast, the CCS/Flat density ($Dsty_{CCS/Flat}$, CCS/Flat number per unit length of flat PM) increased from 0.208 ± 0.006/10 μm at rest to 0.355 ± 0.04/10 μm after KCl application, only ~70% increase (Figure 2C, right).

The much larger $Dsty_{CCS/Inv}$ as compared to $Dsty_{CCS/Flat}$ after KCl application (Figure 2C, black bars), yet similar $\Delta N_{CCS/Inv}$ and $\Delta N_{CCS/Flat}$ (Figure 2B), was because of a much shorter Inv length (Figure 2D, left) as compared to the Flat length (Figure 2D, right). After KCl application, Inv length increased, whereas Flat length decreased slightly (Figure 2D), indicating that KCl induced more membrane invagination. Further supporting this result, KCl application approximately doubled the number of Inv (Figure 2E).

In summary, despite a much smaller membrane length or area (Figure 2D), membrane invaginations were a major platform in generating CCSs (Figures 2A and 2B), because KCl increased the invagination number by ~2 times (Figure 2E) and most importantly increased the $Dsty_{CCS/Inv}$ by ~21 times (Figure 2C, left).

Although the similarity between $\Delta N_{CCS/Inv}$ and $\Delta N_{CCS/Flat}$ (Figures 2A and 2B) suggests a similar contribution of CCS/Inv and CCS/Flat to CCS generation, CCS/Inv's contribution could be underestimated. This was because membrane invaginations were identified at single 70-nm sections, at which Ω-shaped invaginations with a narrow pore beyond the section would appear as an endosome-like structure. Indeed, in experiments where structures were followed in serial sections, seven out of 12 apparently cytosolic endosome-like structures within 400 nm from the PM were connected to the PM in one thin section (example not shown). Thus, our conclusion that CCS/Inv is a major platform for CCS generation is conservative.

KCl stimulation is not as intense as previously assumed

The stimulation used here was high KCl application for 90 s. To estimate how much exocytosis this stimulus generated, we performed confocal imaging of chromaffin cells bathed with Alexa 647 (A647) (Chiang et al., 2014; Wen et al., 2016). Chromaffin cells (cultured at the coverslip) were imaged at the cell bottom membrane (Figure S1A), where fusion was detected as the sudden appearance of A647 spot with A647 fluorescence rising to the peak within ~200 ms, because of diffusion of A647 from the bath solution to the fusion-generated Ω-profiles (Figure S1B) (Chiang et al., 2014; Wen et al., 2016). Application of 90 mM KCl for 90 s induced 37.7 ± 8.4 fusion events per cell at the cell bottom (12 cells, Figure S1C), whereas a 1 s depolarization from −80 to +10 mV induced 10.60 ± 1.36 fusion events (60 cells, Figure S1C). Thus, exocytosis induced by KCl application was about 3.6 times of that induced by a 1-s depolarization from −80 to +10 mV (Chiang et al., 2014; Shin et al., 2018, 2020; Zhao et al., 2016). However, the intensity of exocytosis, calculated as the number of fusion events per unit of time (e.g., per second), was much lower for 90 s KCl application than for 1-s depolarization. Thus, in our conditions, 90 s KCl application was apparently not as strong a stimulus as previously assumed by others.

DISCUSSION

With conventional EM, platinum replica EM, and STED microscopy, we observed clathrin-coated structures (CCS) at both curved plasma membrane invaginations (CCS/Inv) and flat portions of the plasma membrane (CCS/Flat) in primary neuroendocrine chromaffin cells (Figure 1). Similar CCS numbers at membrane invagination ($\Delta N_{CCS/Inv}$) and flat membrane ($\Delta N_{CCS/Flat}$) as induced by KCl (Figures 2A and 2B) suggests that not only flat plasma membranes, but also membrane invaginations are the major site for CCS generation. Challenging the widely held view that CCSs are generated primarily from flat patches of the plasma membrane (Chanaday and Kavalali, 2017; Chanaday et al., 2019; Gan and Watanabe, 2018; Kaksonen and Roux, 2018; Kononenko and Haucke, 2015; Mettlen et al., 2018; Watanabe and Boucrot, 2017; Wu et al., 2014a), our findings suggest modifying this view by including plasma membrane invagination, the precursor for bulk endocytosis, as another major site for clathrin-coated pit and vesicle generation in secretory cells (Figure 2F).

This suggestion is rather surprising, given that the membrane invagination length was much less than that of the flat patches of the PM (Figure 2D). However, KCl-induced depolarizations substantially increased $N_{CCS/Inv}$ by increasing $Dsty_{CCS/Inv}$ by ~21 times (Figure 2C, left) and the invagination number by ~2 times (Figure 2E). The much higher $Dsty_{CCS/Inv}$, as compared to $Dsty_{CCS/Flat}$ after depolarization (Figure 2C, black bars), suggests that CCS prefers to be generated at membrane invaginations with more positive curvature than flat membranes. A positive membrane curvature may thus facilitate clathrin-coated pit generation, because artificially generated positive membrane curvatures are preferred for CCS generation (Zhao et al., 2017). Likewise, in immune B cells and macrophages, clathrin has been shown to form on large invaginations of the plasma membrane (Roberts et al., 2020). We propose that plasma membrane invaginations are a major platform for clathrin-coated pit formation by providing positive curvature, where unique proteins, lipids, tensions, adhesion energies, phases, or cytoskeletal structures may enhance clathrin lattice growth and development. Future work is needed to understand the complex interplay of these cellular factors.

An early study (Takei et al., 1996) three decades ago proposed that clathrin-coated pits/vesicles can be formed at large membrane invaginations (see Introduction). The present work significantly advances the understanding of this proposed pathway by providing quantitative and comprehensive evidence not only supporting this model (Figure 1), but also revealing the importance of this mechanism in retrieving vesicles during depolarization in excitable cells (Figure 2).

As in past studies (Wu et al., 2014b, 2016), here we used KCl solution to induce bulk endocytosis. Physiological action potential trains, such as those induced by optogenetic tools (Watanabe et al., 2013), may ultimately be used in the future to verify our findings. However, the intensity of exocytosis (per unit of time) during 90 s KCl stimulation was much lower than that induced by a 1-s electrical depolarization (Figure S1). EM and capacitance recordings have revealed ultrafast (<~0.6 s), fast (<~5 s) or slow (tens of seconds or more) bulk endocytosis as a dominant endocytic mode after minutes of action potential trains, KCl application, 1–10 pulses of 20-ms depolarization at 10 Hz, 50–200 action potentials at 5–40 Hz, or even single action potentials at a variety of synapses, including calyx of Held synapses, hippocampal synapses, cortical synapses, retinal bipolar cells, and neuromuscular junctions (Heuser and Reese, 1973; Richards et al., 2000; de Lange et al., 2003; Paillart et al., 2003; Wu and Wu, 2007; Watanabe et al., 2013, 2014; Kononenko et al., 2014; Wu et al., 2014b, 2016). Calcium influx, but not the exocytosis amount triggers bulk endocytosis at synapses (Morton et al., 2015; Wu et al., 2009, 2014a). Recently, bulk membrane invaginations have been observed directly in real time in live cells after just a 1-s depolarization, and it is also triggered by calcium influx in chromaffin cells (Shin et al., 2021). Thus, calcium-triggered bulk endocytosis is a major endocytic mechanism in neurons and endocrine cells in both mild and strong stimulation conditions. Our work supports the idea that bulk membrane invagination is a major endocytic route at synapses and endocrine cells in many different physiological conditions.

STED microscopy revealed that in addition to flat-to-Ω shape transitions, fusion-generated Ω-shape membrane profiles may enlarge (termed enlarge fusion) to produce a bulk membrane invaginations (Chiang et al., 2014; Shin et al., 2020). Compound fusion can also produce large invaginations (Nemoto et al., 2001; Hafez et al., 2003; He et al., 2009; Ge et al., 2021). EM-observed bulk membrane invaginations could in principle arise from curvature transitions from flat membranes or from enlarged exocytic fusions. Thus, clathrin-coated pits may be formed at bulk membrane invaginations generated from plasma membrane curvature transitions or enlarged exocytic fusion structures.

Bulk endocytosis has been traditionally thought to serve one purpose – to retrieve a large piece of membrane at once to rapidly enhance endocytosis (illustrated in Figure 2F, left) (Gan and Watanabe, 2018; Kononenko and Haucke, 2015; Wu et al., 2014a). Our results suggest an additional function of bulk endocytosis, to provide a preferred platform—large curved membrane invaginations—for the generation of clathrin-coated pits. We suggest modifying the current classical models of endocytosis to incorporate a close collaboration between two classically independent forms of endocytosis, clathrin-mediated endocytosis and bulk endocytosis (Figure 2F, right).

As illustrated in Figure 2F, our model includes: 1) large membrane invagination serves to mediate not only bulk endocytosis, but also clathrin-coated vesicle endocytosis by providing a preferred platform for clathrin-coated pit and vesicle formation, and 2) bulk endocytosis may generate not only uncoated endosome-like structures, but also endosome-like structures associated with clathrin-coated pits. This model may be of broad application, given that clathrin-mediated endocytosis is essential in eukaryotic cells (Mettlen et al., 2018) and bulk endocytosis is a dominant form of endocytosis in neurons, endocrine cells, and many other cell types (Clayton et al., 2008; Kononenko et al., 2014; Richards et al., 2000; Watanabe et al., 2013; Watanabe and Boucrot, 2017; Wu et al., 2014a; Wu and Wu, 2007).

Limitations of the study

Our suggestion that clathrin-coated pit pinches off from bulk membrane invagination after high KCl stimulation is based on EM that does not provide the dynamics of the vesicle scission or internalization. Direct observation of this dynamic process with high temporal-resolution and spatial-resolution light imaging is a future direction and is ultimately needed to verify and solidify the main suggestion of the present work.

STAR★METHODS

Detailed methods are provided in the online version of this paper and include the following:

- KEY RESOURCES TABLE
- RESOURCE AVAILABILITY
  - Lead contact
  - Materials availability
  - Data and code availability
- EXPERIMENTAL MODEL AND SUBJECT DETAILS
  - Primary cell culture
- METHOD DETAILS
  - Chromaffin cell culture
  - Conventional electron microscopy
  - Unroofing, platinum replica coating and electron microscopy
  - Electroporation and plating
  - Plasmids and fluorescent dyes
  - STED imaging
  - Confocal imaging
  - Electrophysiology
- QUANTIFICATION AND STATISTICAL ANALYSIS
  - Data selection and statistics

SUPPLEMENTAL INFORMATION

Supplemental information can be found online at https://doi.org/10.1016/j.isci.2022.103809.

ACKNOWLEDGMENTS

This work was supported by the National Institute of Neurological Disorders and Stroke Intramural Research Program (ZIA NS003009-15 and ZIA NS003105-10 to L.G.W.), and the Intramural Research Program of the National Heart, Lung, and Blood Institute (J.W.T.); U.A. was supported by the ISF-NSFC 2546/16 and Israel Science Foundation grant 2141/20; O.S. was supported by the Swedish Research Council grant 1731, Fernström's Stiftelse, and the Russian Science Foundation grant 21-15-00227; G.A. received stipends and support from the Karolinska Institutet-NIH Doctoral Partnership Program in Neuroscience,

Fernstrom's Stiftelse, and Karolinska Institutet funds. We thank Susan Cheng (National Institute of Neurological Disorders and Stroke), Christopher Bleck (National Heart, Lung, and Blood Institute) for electron microscopy (EM) support, Kem A Sochacki (National Heart, Lung, and Blood Institute) for advice on platinum replica EM, and Ethan Tyler (NIH Medical Arts) for helping to create Figure 2F.

AUTHOR CONTRIBUTIONS

G.A. designed experiments, performed EM and imaging experiments with help from O.S., and S.V. L.G. and C.Y.C. performed preliminary imaging experiments important for the development of imaging results presented here. W.S. performed confocal imaging related to high potassium experiments. A.S. did platinum replica EM with help from G.A. and U.A. L.G.W., U.A., O.S., and J. T. designed and supervised the project. G.A. and L.G.W. wrote the manuscript with help from others.

DECLARATION OF INTERESTS

The authors declare no competing interests.

Received: April 1, 2021
Revised: June 2, 2021
Accepted: January 20, 2022
Published: February 18, 2022

REFERENCES

Ai, H.W., Olenych, S.G., Wong, P., Davidson, M.W., and Campbell, R.E. (2008). Hue-shifted monomeric variants of clavularia cyan fluorescent protein: identification of the molecular determinants of color and applications in fluorescence imaging. BMC Biol. *6*, 13.

Chanaday, N.L., Cousin, M.A., Milosevic, I., Watanabe, S., and Morgan, J.R. (2019). The synaptic vesicle cycle revisited: new insights into the modes and mechanisms. J. Neurosci. *39*, 8209–8216.

Chanaday, N.L., and Kavalali, E.T. (2017). How do you recognize and reconstitute a synaptic vesicle after fusion? F1000Res. *6*, 1734.

Chiang, H.C., Shin, W., Zhao, W.D., Hamid, E., Sheng, J., Baydyuk, M., Wen, P.J., Jin, A., Momboisse, F., and Wu, L.G. (2014). Post-fusion structural changes and their roles in exocytosis and endocytosis of dense-core vesicles. Nat. Commun. *5*, 3356.

Clayton, E.L., Evans, G.J., and Cousin, M.A. (2008). Bulk synaptic vesicle endocytosis is rapidly triggered during strong stimulation. J. Neurosci. *28*, 6627–6632.

de Lange, R.P., de Roos, A.D., and Borst, J.G. (2003). Two modes of vesicle recycling in the rat calyx of held. J. Neurosci. *23*, 10164–10173.

Ferguson, S.M., Brasnjo, G., Hayashi, M., Wolfel, M., Collesi, C., Giovedi, S., Raimondi, A., Gong, L.W., Ariel, P., Paradise, S., et al. (2007). A selective activity-dependent requirement for dynamin 1 in synaptic vesicle endocytosis. Science *316*, 570–574.

Fotin, A., Cheng, Y., Sliz, P., Grigorieff, N., Harrison, S.C., Kirchhausen, T., and Walz, T. (2004). Molecular model for a complete clathrin lattice from electron cryomicroscopy. Nature *432*, 573–579.

Gan, Q., and Watanabe, S. (2018). Synaptic vesicle endocytosis in different model systems. Front. Cell Neurosci. *12*, 171.

Ge, L., Shin, W., and Wu, L.-G. (2021). Visualizing sequential compound fusion and kiss-and-run in live excitable cells. bioRxiv. https://doi.org/10.1101/2021.06.21.449230.

Hafez, I., Stolpe, A., and Lindau, M. (2003). Compound exocytosis and cumulative fusion in eosinophils. J. Biol. Chem. *278*, 44921–44928.

He, L., Xue, L., Xu, J., McNeil, B.D., Bai, L., Melicoff, E., Adachi, R., and Wu, L.G. (2009). Compound vesicle fusion increases quantal size and potentiates synaptic transmission. Nature *459*, 93–97.

Heuser, J.E., and Reese, T.S. (1973). Evidence for recycling of synaptic vesicle membrane during transmitter release at the frog neuromuscular junction. J. Cell Biol. *57*, 315–344.

Hirokawa, N., and Heuser, J.E. (1981). Quick-freeze, deep-etch visualization of the cytoskeleton beneath surface differentiations of intestinal epithelial-cells. J. Cell Biol. *91*, 399–409.

Kaksonen, M., and Roux, A. (2018). Mechanisms of clathrin-mediated endocytosis. Nat. Rev. Mol. Cell Biol. *19*, 313–326.

Kononenko, N.L., and Haucke, V. (2015). Molecular mechanisms of presynaptic membrane retrieval and synaptic vesicle reformation. Neuron *85*, 484–496.

Kononenko, N.L., Puchkov, D., Classen, G.A., Walter, A.M., Pechstein, A., Sawade, L., Kaempf, N., Trimbuch, T., Lorenz, D., Rosenmund, C., et al. (2014). Clathrin/AP-2 mediate synaptic vesicle reformation from endosome-like vacuoles but are not essential for membrane retrieval at central synapses. Neuron *82*, 981–988.

Lomasney, J.W., Cheng, H.F., Wang, L.P., Kuan, Y., Liu, S., Fesik, S.W., and King, K. (1996). Phosphatidylinositol 4,5-bisphosphate binding to the pleckstrin homology domain of phospholipase C-delta1 enhances enzyme activity. J. Biol. Chem. *271*, 25316–25326.

Ludwig, A., Nichols, B.J., and Sandin, S. (2016). Architecture of the caveolar coat complex. J. Cell Sci. *129*, 3077–3083.

Mastronarde, D.N. (2005). Automated electron microscope tomography using robust prediction of specimen movements. J. Struct. Biol. *152*, 36–51.

Mettlen, M., Chen, P.H., Srinivasan, S., Danuser, G., and Schmid, S.L. (2018). Regulation of clathrin-mediated endocytosis. Annu. Rev. Biochem. *87*, 871–896.

Morton, A., Marland, J.R., and Cousin, M.A. (2015). Synaptic vesicle exocytosis and increased cytosolic calcium are both necessary but not sufficient for activity-dependent bulk endocytosis. J. Neurochem. *134*, 405–415.

Nemoto, T., Kimura, R., Ito, K., Tachikawa, A., Miyashita, Y., Iino, M., and Kasai, H. (2001). Sequential-replenishment mechanism of exocytosis in pancreatic acini. Nat. Cell Biol. *3*, 253–258.

Paillart, C., Li, J., Matthews, G., and Sterling, P. (2003). Endocytosis and vesicle recycling at a ribbon synapse. J. Neurosci. *23*, 4092–4099.

Parton, R.G., Tillu, V.A., and Collins, B.M. (2018). Caveolae. Curr. Biol. *28*, R402–R405.

Peiro, S., Comella, J.X., Enrich, C., Martin-Zanca, D., and Rocamora, N. (2000). PC12 cells have caveolae that contain TrkA. Caveolae-disrupting drugs inhibit nerve growth factor-induced, but not epidermal growth factor-induced, MAPK phosphorylation. J. Biol. Chem. *275*, 37846–37852.

Richards, D.A., Guatimosim, C., and Betz, W.J. (2000). Two endocytic recycling routes selectively fill two vesicle pools in frog motor nerve terminals. Neuron *27*, 551–559.

Roberts, A.D., Davenport, T.M., Dickey, A.M., Ahn, R., Sochacki, K.A., and Taraska, J.W. (2020). Structurally distinct endocytic pathways for B cell receptors in B lymphocytes. Mol. Biol. Cell *31*, 2826–2840.

Saheki, Y., and De Camilli, P. (2012). Synaptic vesicle endocytosis. Cold Spring Harb. Perspect. Biol. *4*, a005645.

Schindelin, J., Arganda-Carreras, I., Frise, E., Kaynig, V., Longair, M., Pietzsch, T., Preibisch, S., Rueden, C., Saalfeld, S., Schmid, B., et al. (2012). Fiji: an open-source platform for biological-image analysis. Nat. Methods *9*, 676–682.

Sharma, S., and Lindau, M. (2018). The fusion pore, 60 years after the first cartoon. FEBS Lett. *592*, 3542–3562.

Shin, W., Arpino, G., Thiyagarajan, S., Su, R., Ge, L., McDargh, Z., Guo, X., Wei, L., Shupliakov, O., Jin, A., et al. (2020). Vesicle shrinking and enlargement play opposing roles in the release of exocytotic contents. Cell Rep. *30*, 421–431.e7.

Shin, W., Ge, L., Arpino, G., Villarreal, S.A., Hamid, E., Liu, H., Zhao, W.D., Wen, P.J., Chiang, H.C., and Wu, L.G. (2018). Visualization of membrane pore in live cells reveals a dynamic-pore theory governing fusion and endocytosis. Cell *173*, 934–945.

Shin, W., Wei, L., Arpino, G., Ge, L., Guo, X., Chan, C.Y., Hamid, E., Shupliakov, O., Bleck, C.K.E., and Wu, L.G. (2021). Preformed omega-profile closure and kiss-and-run mediate endocytosis and diverse endocytic modes in neuroendocrine chromaffin cells. Neuron *109*, 3119–3134.e5.

Smith, C., and Neher, E. (1997). Multiple forms of endocytosis in bovine adrenal chromaffin cells. J. Cell Biol. *139*, 885–894.

Sochacki, K.A., Dickey, A.M., Strub, M.P., and Taraska, J.W. (2017). Endocytic proteins are partitioned at the edge of the clathrin lattice in mammalian cells. Nat. Cell Biol. *19*, 352–361.

Sochacki, K.A., Heine, B.L., Haber, G.J., Jimah, J.R., Prasai, B., Alfonzo-Mendez, M.A., Roberts, A.D., Somasundaram, A., Hinshaw, J.E., and Taraska, J.W. (2021). The structure and spontaneous curvature of clathrin lattices at the plasma membrane. Dev. Cell *56*, 1131–1146.e3.

Sochacki, K.A., Larson, B.T., Sengupta, D.C., Daniels, M.P., Shtengel, G., Hess, H.F., and Taraska, J.W. (2012). Imaging the post-fusion release and capture of a vesicle membrane protein. Nat. Commun. *3*, 1154.

Sochacki, K.A., Shtengel, G., van Engelenburg, S.B., Hess, H.F., and Taraska, J.W. (2014). Correlative super-resolution fluorescence and metal-replica transmission electron microscopy. Nat. Methods *11*, 305–U278.

Takei, K., Mundigl, O., Daniell, L., and De Camilli, P. (1996). The synaptic vesicle cycle: a single vesicle budding step involving clathrin and dynamin. J. Cell Biol. *133*, 1237–1250.

Varnai, P., and Balla, T. (1998). Visualization of phosphoinositides that bind pleckstrin homology domains: calcium- and agonist-induced dynamic changes and relationship to myo-[3H]inositol-labeled phosphoinositide pools. J. Cell Biol. *143*, 501–510.

Watanabe, S., and Boucrot, E. (2017). Fast and ultrafast endocytosis. Curr. Opin. Cell Biol. *47*, 64–71.

Watanabe, S., Rost, B.R., Camacho-Perez, M., Davis, M.W., Sohl-Kielczynski, B., Rosenmund, C., and Jorgensen, E.M. (2013). Ultrafast endocytosis at mouse hippocampal synapses. Nature *504*, 242–247.

Watanabe, S., Trimbuch, T., Camacho-Perez, M., Rost, B.R., Brokowski, B., Sohl-Kielczynski, B., Felies, A., Davis, M.W., Rosenmund, C., and Jorgensen, E.M. (2014). Clathrin regenerates synaptic vesicles from endosomes. Nature *515*, 228–233.

Wen, P.J., Grenklo, S., Arpino, G., Tan, X., Liao, H.S., Heureaux, J., Peng, S.Y., Chiang, H.C., Hamid, E., Zhao, W.D., et al. (2016). Actin dynamics provides membrane tension to merge fusing vesicles into the plasma membrane. Nat. Commun. *7*, 12604.

Wu, L.G., Hamid, E., Shin, W., and Chiang, H.C. (2014a). Exocytosis and endocytosis: modes, functions, and coupling mechanisms. Annu. Rev. Physiol. *76*, 301–331.

Wu, W., and Wu, L.G. (2007). Rapid bulk endocytosis and its kinetics of fission pore closure at a central synapse. Proc. Natl. Acad. Sci. U S A *104*, 10234–10239.

Wu, X.S., Lee, S.H., Sheng, J., Zhang, Z., Zhao, W.D., Wang, D., Jin, Y., Charnay, P., Ervasti, J.M., and Wu, L.G. (2016). Actin is crucial for all kinetically distinguishable forms of endocytosis at synapses. Neuron *92*, 1020–1035.

Wu, X.S., McNeil, B.D., Xu, J., Fan, J., Xue, L., Melicoff, E., Adachi, R., Bai, L., and Wu, L.G. (2009). Ca(2+) and calmodulin initiate all forms of endocytosis during depolarization at a nerve terminal. Nat. Neurosci. *12*, 1003–1010.

Wu, Y., O'Toole, E.T., Girard, M., Ritter, B., Messa, M., Liu, X., McPherson, P.S., Ferguson, S.M., and De Camilli, P. (2014b). A dynamin 1-, dynamin 3- and clathrin-independent pathway of synaptic vesicle recycling mediated by bulk endocytosis. eLife *3*, e01621.

Zhao, W.D., Hamid, E., Shin, W., Wen, P.J., Krystofiak, E.S., Villarreal, S.A., Chiang, H.C., Kachar, B., and Wu, L.G. (2016). Hemi-fused structure mediates and controls fusion and fission in live cells. Nature *534*, 548–552.

Zhao, W.T., Hanson, L., Lou, H.Y., Akamatsu, M., Chowdary, P.D., Santoro, F., Marks, J.R., Grassart, A., Drubin, D.G., Cui, Y., et al. (2017). Nanoscale manipulation of membrane curvature for probing endocytosis in live cells. Nat. Nanotechnol. *12*, 750–756.

STAR★METHODS

KEY RESOURCES TABLE

REAGENT or RESOURCE	SOURCE	IDENTIFIER
Chemicals, peptides, and recombinant proteins		
DMEM medium	Gibco	Cat#11885092
Fetal bovine serum	Gibco	Cat#10082147
German glass coverslips with mouse Laminin coating over PDL layer	Neuvitro	GG-25-Laminin; GG-25-1.5-Laminin
Trypsin inhibitor	Sigma	T9253; CAS: 9035-81-8
Alexa 647	Sigma	A20502
Bovine serum albumin	Sigma	A2153; CAS: 9048-46-8
Tannic Acid	Sigma	403040
Embed-812	EMS	Cat#13940
Collagenase P	Sigma	COLLP-RO Roche 11249002001
Critical commercial assays		
Basic Primary Neurons Nucleofector Kit	Lonza	Cat#VVPI-1003
Experimental models: Primary cell culture		
Bovine adrenal chromaffin cell	J. W. Treuth and Sons, Inc.	Adrenal Glands
Recombinant DNA		
Clathrin-mTFP1	Ai et al., 2008	Addgene Plasmid #55471
mNeonGreen	Allele Biotechnology	ABP-FP-MNEONSB
PH-mNeonGreen	Shin et al., 2018	Allele Biotechnology
PH-EGFP	Varnai and Balla (1998)	Addgene Plasmid #51407
Software and algorithms		
Huygens Professional	Scientific Volume Imaging	https://svi.nl/Huygens-Professional
Image J	NIH	https://imagej.nih.gov/ij/
LAS X	Leica	https://www.leicabiosystems.com/
Prism	GraphPad	https://www.graphpad.com/scientific-software/prism/

RESOURCE AVAILABILITY

Lead contact

Further information and requests for resources and reagents should be directed to and will be fulfilled by the Lead Contact Ling-Gang Wu (wul@ninds.nih.gov).

Materials availability

This study did not generate new unique reagents.

Data and code availability

All data reported in this paper will be shared by corresponding authors upon request.

This paper does not report original code.

Any additional information required to reanalyze the data reported in this paper is available from corresponding authors upon request.

EXPERIMENTAL MODEL AND SUBJECT DETAILS

Primary cell culture

Fresh adult (21–27 months old) male bovine adrenal glands purchased from a local abattoir (J. W. Treuth and Sons, Inc.) were used to prepare primary chromaffin cell culture, which are widely used for the study of exo- and endocytosis (Wu et al., 2014a; Sharma and Lindau, 2018).

METHOD DETAILS

Chromaffin cell culture

To prepare for primary bovine chromaffin cell cultures (Chiang et al., 2014; Wen et al., 2016), we obtained fresh adult bovine adrenal glands from a local slaughterhouse. Fresh adrenal glands were immersed in pre-chilled Locke's buffer on ice containing the following: NaCl, 145 mM; KCl, 5.4 mM; Na_2HPO_4, 2.2 mM; NaH_2PO_4, 0.9 mM; glucose, 5.6 mM; HEPES, 10 mM (pH 7.3, adjusted with NaOH). The excess fat was trimmed off, and the glands were perfused with Locke's buffer. Each gland was then infused through the portal vein with Locke's buffer containing collagenase P (1.5 mg/mL, Roche), trypsin inhibitor (0.325 mg/mL, Sigma), and bovine serum albumin (5 mg/mL, Sigma), and incubated at 37°C for 20 min in a water bath. A longitudinal cut was made on the gland to expose the medulla that was then minced in Locke's buffer and filtered through a 100- μm nylon mesh. The supernatant was discarded, the pellet centrifuged (48 × g, 5 min), re-suspended in Locke's buffer and re-centrifuged until the supernatant was clear. The final cell pellet was re-suspended in a pre-warmed DMEM low glucose medium (GIBCO) supplemented with 10% fetal bovine serum (GIBCO). The plated cells were incubated at 37°C, 8% humidified CO_2 and used 2/3 after the culture.

Conventional electron microscopy

For the rest condition, bovine chromaffin cells were fixed with 2% glutaraldehyde, 2% paraformaldehyde, and 4% tannic acid in 0.1 M cacodylate buffer pH 7.4 for 15 min, followed by the same fixative without tannic acid for an additional 15 min (Shin et al., 2018). For the stimulation protocol the cells were immersed for 90 s in a solution containing 70 mM KCl, 60 mM NaCl, 10 mM glucose, 10 mM HEPES, 2 mM $CaCl_2$, and 1 mM $MgCl_2$ (pH 7.3, adjusted with NaOH) before the fixation. Once fixed, the cells were rinsed with 100 mM glycine solution in 0.1 M sodium cacodylate buffer for 1 min at room temperature, and then with 0.1 M sodium cacodylate. After post-fixation with 1% OsO_4 for 1 h on ice, the samples were dehydrated in 50 and 70% ethanol, stained en-bloc in 2% Uranyl acetate in 70% ethanol, and then dehydrated in 85%, 95%, and 100% ethanol (30 min for each incubation). The samples were embedded in Embed-812 (Electron Microscopy Sciences). Single and serial ultrathin sections (70–90 nm) were prepared in an ultramicrotome (Leica) using a diamond knife (Diatome) and placed onto 200 mesh pioloform coated index grids. Single images were collected in a JEOL JEM-200 C × 120 kV electron microscope equipped with an AMT XR-100 CCD.

The quantification of the event frequency from single sections was done using the software ImageJ (Schindelin et al., 2012). The number of clathrin-coated structures (CCS) on the membrane invagination (Inv, height >300 nm; Inv, base < 3× Inv height) and flat plasma membrane (PM) were counted from 40 cell cross sections. The number of CCS/Inv ($N_{CCS/Inv}$) and CCS/Flat ($N_{CCS/Flat}$) were calculated per unit length of PM. We set the unit as 10 μm. The net increase of $N_{CCS/Inv}$ by the 70 mM KCl application ($\Delta N_{CCS/Inv}$) was calculated as $N_{CCS/Inv}$ after KCl application subtracted by the mean $N_{CCS/Inv}$ obtained at the resting condition. Similarly, the net increase of $N_{CCS/Flat}$ by the KCl application ($\Delta N_{CCS/Flat}$) was calculated as $N_{CCS/Flat}$ after KCl application subtracted by the mean $N_{CCS/Flat}$ obtained at the resting condition. CCS/Inv density ($Dsty_{CCS/Inv}$) was calculated as the number of CCS/Inv per unit length of Inv; similarly, CCS/Flat density ($Dsty_{CCS/Flat}$) was calculated as the number of CCS/Flat per unit length of flat PM (the unit length was set as 10 μm). The percentage of Inv length was calculated as the Inv length divided by the total length of the PM (including Inv and flat PM) for the cell at the thin section. Similarly, the percentage of the flat PM length was calculated as the flat PM length divided by the total PM length. The number of Inv (N_{Inv}) was calculated as the number of Inv per unit (10 μm) length of PM.

In some experiments, apparent endosome-like structures within 400 nm from the plasma membrane were followed by serial ultrathin sections at transmission electron microscopy (TEM) to determine whether they are connected with the plasma membrane. For statistical analysis, significance and p-values were calculated using unpaired Student's t-test (two-tailed).

The presence of a distinct coat in TEM images quantified here was the major argument that it contained clathrin. These coats appeared to be composed of lattices containing pentagons and hexagons as revealed by our platinum replica EM in chromaffin cells (Figures 1F–1H). Such organization of coats is in good agreement with the well-known properties of clathrin, the only coat protein that may form such structures (Fotin et al., 2004). Other coat proteins, caveolins, have been linked to the endocytic vesicle formation from the plasma membrane in different cell types (Parton et al., 2018). Caveolae are abundant structures observed in adipocytes, skeletal muscle cells, endothelia, and fibroblasts but undetectable in some other cell types such as neurons (Ludwig et al., 2016; Parton et al., 2018; Peiro et al., 2000). In secretory cells, they may exist, but are rare (Peiro et al., 2000), which was confirmed by the platinum replica EM in chromatin cells (Figures 1F–1H). Importantly, caveolae do not possess the prominent coat structure typical to clathrin-coated pits in classical transmission electron microscopic images and thus could be selected away (Peiro et al., 2000; Ludwig et al., 2016; Parton et al., 2018). We concluded that the coated membrane identified here reflects clathrin-coated membrane.

Unroofing, platinum replica coating and electron microscopy

Cells were stimulated immerging the coverslip for 45 s in a solution containing 70 mM KCl, 60 mM NaCl, 10 mM glucose, 10 mM HEPES, 2 mM $CaCl_2$, and 1 mM MgCl2 (pH 7.3, adjusted with NaOH), transferred to stabilization buffer (2 mL) (70 mM KCl, 30 mM HEPES, 5 mM $MgCl_2$, 3 mM EGTA at pH 7.4) and immediately unroofed and fixed splashing them with a syringe containing a final solution of stabilization buffer and 2% paraformaldehyde. The coverslips were then transferred in 2% glutaraldehyde in stabilization buffer and incubated at 4°C for 20 min. Afterwards, cells were moved to 0.1% w/v tannic acid (freshly dissolved in water) for 20 min. They were then rinsed 4× with water and placed in 0.1% w/v uranyl acetate for 20 min. The coverslips were then dehydrated, critical point dried, and coated with platinum and carbon as previously described (Sochacki et al., 2012). The region of interest on the coverslip was imaged with 10 × phase contrast to obtain a map of the imaged region. The replicas were lifted as previously described (Sochacki et al., 2014) and placed onto Formvar/carbon-coated 75-mesh copper TEM grids (Ted Pella 01802-F) that were recently glow-discharged. Some cells were lost behind grid bars. TEM imaging was performed as previously described at 15,000x magnification (1.2 nm per pixel) using a JEOL 1400 and SerialEM freeware for montaging (Mastronarde, 2005). Images are presented in inverted contrast.

Electroporation and plating

Cells were transfected by electroporation using a basic neurons nucleofector Kit (Lonza, program O-005), according to the manufacturer's protocol. Then, they were then plated onto precoated glass coverslips [poly-L-lysine (0.005% w/v, Sigma) and laminin (4 mg/mL, Sigma)]. The cells were incubated at 37°C with 8% CO_2 and used within 5 days.

Plasmids and fluorescent dyes

PH-mNeonGreen (phospholipase C delta PH domain attached with mNeonGreen) construct was created by replacing the EGFP tag of PH-EGFP (Varnai and Balla, 1998) obtained from Dr. Tamas Balla (NICHD, Bethesda, USA) with mNeonGreen (Allele Biotechnology) (Shin et al., 2018). Clathrin-mTFP1 construct was purchased from Addgene (Ai et al., 2008).

STED imaging

STED images were acquired with Leica TCS SP8 STED 3 × microscope that is equipped with a 100 3 1.4 NA HC PL APO CS2 oil immersion objective and operated with the LAS-X imaging software (Shin et al., 2018; Zhao et al., 2016). Excitation was with a tunable white light laser and emission was detected with hybrid detectors. PH-mNeonGreen and Clathrin-mTFP1 were sequentially excited at 485 and 434 nm, respectively, with the 592 nm STED depletion beam, and their fluorescence collected at 495–530 nm and 447–490 nm, respectively. STED imaging generally causes more photobleaching and phototoxicity. STED images were acquired at the cell bottom with XZ (perpendicular to the coverslip) scanning mode. For XY/Zfix scanning (Z focal plane was fixed at ~100–200 nm above the cell. The STED resolution for imaging PH-mNeonGreen in our conditions was ~60 nm on the microscopic X- and Y axis (parallel to cell-bottom membrane or coverslip), and ~150–200 nm on the microscopic z axis. STED images were deconvolved using Huygens software (Scientific Volume Imaging).

Confocal imaging

With an inverted confocal microscope (TCS SP5II, Leica, Germany, 100× oil objective, numerical aperture: 1.4), A647 (30 μM in bath, Invitrogen) was excited by a HeNe laser at 633 nm (maximum power: 20 mW). The 633 nm laser was set at 60% of the maximum power. A647 fluorescence was collected with a photomultiplier at 643–700 nm. Confocal imaging area was ~70–160 μm^2. Images were collected every 5–15 ms at 50–70 nm per pixel. Fusion was detected as the sudden appearance of A647 spot with A647 fluorescence rising to the peak within ~200 ms because of diffusion of A647 from the bath solution to the fusion-generated Ω-profiles (Figure S1) (Chiang et al., 2014; Wen et al., 2016).

Electrophysiology

The stimulation we used was either 90 mM KCl for 90 s or a 1 s depolarization from −80 to +10 mV at the whole-cell voltage-clamp configuration. Whole-cell voltage-clamp and capacitance recordings were performed with an EPC-10 amplifier together with the software lock-in amplifier (PULSE, HEKA, Lambrecht, Germany) at room temperature (22–24°C) (Chiang et al., 2014). The holding potential was −80 mV. The frequency of the sinusoidal stimulus was 1,000–1,500 Hz with a peak-to-peak voltage ≤50 mV. The bath solution contained 125 mM NaCl, 10 mM glucose, 10 mM HEPES, 5 mM $CaCl_2$, 1 mM $MgCl_2$, 4.5 mM KCl, 0.001 mM TTX and 20 mM TEA, pH 7.3 adjusted with NaOH. The pipette (3–6 MΩ) solution contained 130 mM Cs-glutamate, 0.5 mM Cs-EGTA, 12 mM NaCl, 30 mM HEPES, 1 mM $MgCl_2$, 2 mM ATP, and 0.5 mM GTP, pH 7.2 adjusted with CsOH. These solutions pharmacologically isolated calcium currents.

QUANTIFICATION AND STATISTICAL ANALYSIS

Data selection and statistics

For confocal imaging, data within the first 2 min after whole-cell break-in were used to avoid whole-cell endocytosis rundown (Chiang et al., 2014; Smith and Neher, 1997). Cell selection was not random, but based on the footprint image and the experience accumulated in the last decade. The statistical test used is t test. The significance level was set at $p < 0.05$. The data were expressed as mean ± SEM Each group of data was from at least three primary chromaffin cell cultures. Each culture was from 2-4 glands from 1-2 bovine. We determined these sample-sizes based on the experience in the last ten years. Blinding was not used for data collection or analysis. Bovine selection was blinded, because they were selected by workers in the abattoir without our participation.